Interactions and phase transformations in Fe-Pd

C. R. Sax,[1] B. Schönfeld,[1] and A. V. Ruban[2]
[1]*Laboratory of Metal Physics and Technology, Department of Materials, ETH Zurich, 8093 Zurich, Switzerland*
[2]*Department of Materials Science and Engineering, Royal Institute of Technology, 10044 Stockholm, Sweden*
(Received 18 October 2013; revised manuscript received 22 December 2013; published 13 January 2014)

Interactions in Fe-Pd were studied using diffuse x-ray scattering and first-principles calculations. Diffuse x-ray scattering was performed from single crystals of Fe–38.2 at. % Pd and Fe–81.0 at. % Pd to investigate states of thermal equilibrium at 1023 K and 1073 K, respectively. Short-range-order scattering was separated and effective pair interaction (EPI) parameters were determined using the inverse Monte Carlo method. The EPI parameters are found to strongly vary with respect to data from a previous investigation of Fe–50 at. % Pd. Electronic-structure calculations of effective cluster interaction (ECI) parameters for these states showed the importance of considering multibody interactions and applying the disordered local moment model of the magnetic state: in the ferromagnetic model, the strength of the interactions gets overestimated. Close agreement is reached for short-range order between calculations and the present scattering experiments. Using either a linear compositional variation of the EPI parameters or ECI parameters for alloys with other Pd fractions, the shape of the order-disorder transition line on the Pd-rich side could be reproduced.

DOI: 10.1103/PhysRevB.89.014201 PACS number(s): 64.60.Cn, 71.15.−m, 75.50.Bb

I. INTRODUCTION

The Fe-Pd phase diagram is characterized by a contiguous high-temperature γ solid solution [1]. Two ordered phases are experimentally known (see Fig. 1), the γ_1 phase with $L1_0$ superstructure (FePd) and the γ_2 phase with $L1_2$ superstructure ($FePd_3$). On the Fe-rich side there is a broad miscibility gap, due to a positive heat of mixing [2]. Still, Fe_3Pd with $L1_2$ superstructure has been noted to exist either as a metastable state or for nanoparticles [3,4].

On the basis of total energies of about 100 fully relaxed ordered compounds in the high-spin state, an exhaustive ground-state search was done by Barabash *et al.* [5] and Chepulskii *et al.* [6] using a cluster expansion method. Barabash *et al.* [5] found $FePd_2$, Fe_3Pd_9, and $FePd_8$ as possible new compounds. It could not be settled whether $L1_0$ is unstable as a ground-state structure or not: the finding that the γ_1 phase extends barely below 50 at. % Pd, but reaches up to about 60 at. % Pd, was considered as an indicator for a possible different ordered structure or decomposition at low temperatures. In a subsequent comprehensive study Chepulskii *et al.* [6] still presented more ground states, Fe_2Pd_7, $FePd_5$, and Fe_2Pd_{13}. These structures, however, were finally not counted as ground states as their formation enthalpy was not deep, i.e., only less than 1 meV per atom below the convex hull. Like Barabash *et al.* [5], Chepulskii *et al.* [6] found $FePd_3$ ($L1_2$) not to be a stable ground-state structure. Even at elevated temperatures it should not be stable, in contrast to experimental findings. No reason could be provided.

A remarkable feature in the Fe-Pd phase diagram is the large shift of the congruent ordering of the γ_1 and γ_2 phases; from the 1:1 stoichiometry (γ_1) to Fe–59 at. % Pd with an order-disorder transition temperature of 1063(20) K and from the 1:3 stoichiometry (γ_2) to 66 at. % Pd with 1093(20) K [7]. More recently, Takezawa *et al.* [8] closely confirmed these data, together with the presence of an intermediate two-phase region ranging from about 60 to 63 at. % Pd.

Mohri *et al.* [9,10] attempted to model the phase boundary of the γ_1 phase. Employing a Lennard-Jones potential for the interatomic interactions and the cluster variation method (CVM), they found that the tetragonality of $L1_0$ leads to a shift in the congruent ordering to a temperature closer to the experimental value [9]. Later on Mohri and Chen [10] performed total energy electronic-structure calculations and used the cluster expansion method to obtain interaction parameters. Employing the cluster variation method (CVM), the temperature of congruent ordering matched the experimental results. A shift away from the 1:1 stoichiometry, however, could not be reproduced.

Based on diffuse scattering, ordering temperatures may be determined. Such a procedure was successfully applied, especially when a cubic-cubic order-disorder transformation takes place (for a compilation of those data, see Schönfeld [11]). Such an approach was also followed by Mehaddene *et al.* [12] for Fe–50 at. % Pd kept in solid solution at 1020 K. Using diffuse neutron scattering on a time-of-flight (TOF) instrument, the elastic scattering of (100) and (110) planes was determined. Short-range-order scattering was separated, and using the inverse Monte Carlo method effective pair interaction (EPI) parameters were obtained [13]. An order-disorder transition temperature of 705 (160) K was obtained, about 250 K lower than the experimental value. It was judged by Mehaddene [13] that this difference might be largely attributed to the uncertainty of the EPI parameters. Note also that FePd is tetragonal with a lattice parameter ratio c/a of 0.97 (see Hultgren and Zapfe [14]) that will stabilize the ordered state. This point was not further considered in this work.

EPI parameters may depend on composition and temperature. For their determination by diffuse scattering, a state of thermal equilibrium must be investigated, at best within the solid solution. The large shift in congruent ordering on the Pd-rich side of Fe-Pd is taken as an indicator for a large compositional dependence of the EPI parameters. Thus, Fe–81.0 at. % Pd was chosen for a diffuse x-ray scattering experiment to allow a comparison with Fe–50 at. % Pd previously studied by Mehaddene *et al.* [12]. A strict difference to Fe–50 at. % Pd is expected where a negative value of the nearest-neighbor EPI parameter was obtained thus

 ©2014 American Physical Society

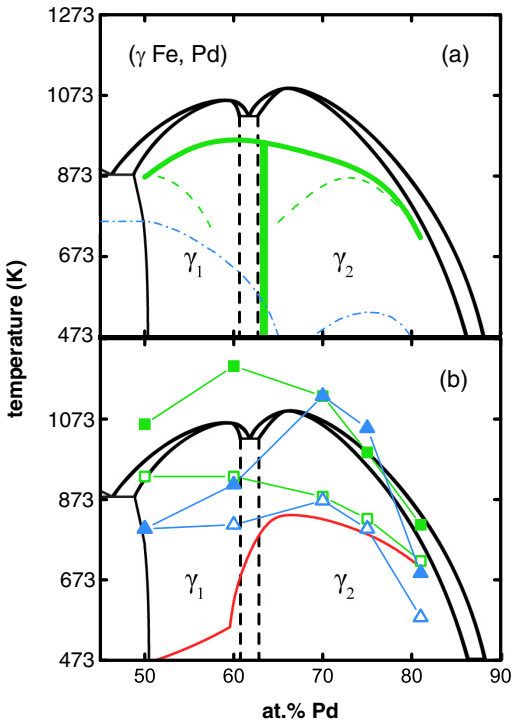

FIG. 1. (Color online) Pd-rich side of the Fe-Pd phase diagram according to Okamoto [1] (black lines). (a) The order-disorder transition line, together with the location of the γ_1-γ_2 two-phase regime, were determined from the composition-dependent (linearly interpolated) EPI parameters from diffuse scattering (green, straight line; estimated uncertainty: ±50 K) and also from the composition-independent EPI parameters from Fe–50 at. % Pd and Fe–81 at. % Pd of Table IV (green, dashed line). In addition, the Curie temperature is shown (blue, dashed-dotted line). (b) Same as with (a) but using the ECI parameters in the DLM (triangles) and FM (squares) states from electronic-structure calculations (open symbols: only $V_p^{(2)}$, filled symbols: with all ECI parameters). Lines are drawn to guide the eyes. Also shown (red line) is the result redrawn from the calculations of Chepulskii *et al.* [6].

indicating a tendency towards local decomposition (although short-range-order scattering exhibits maxima at 100 positions, indicating a tendency towards local order). To the authors' knowledge no large shift in congruent ordering has yet been modeled on the basis of the concentration dependence of EPI parameters from experiment.

To note whether the EPI parameters in Fe-Pd display a smooth variation with composition as, e.g., seen in the Ni-Pt system [15], another composition needs to be investigated. Fe–38.2 at. % Pd was chosen for two reasons: (i) at Pd fractions larger than 32 at. % no martensitic transformation was observed [16] above room temperature that might affect a structural investigation, and (ii) the solid solution starts at ∼950 K which is supposed to be sufficiently low to quench in a state of thermal equilibrium for a diffuse scattering experiment at room temperature.

There is also a strong need to perform first-principles calculations. Recent calculations [6] were based on interactions within the ferromagnetic state. They failed to reproduce the phase diagram in two respects: (i) they failed to confirm the $L1_2$ structure of one of the two experimentally established ordered phases, the γ_2 phase, and (ii) they did not reproduce the known order-disorder transition temperature of the other ordered phase (γ_1). It seems worth considering that the phase transitions occur in the paramagnetic state.

The present work is set up as a combined experimental and theoretical approach to understand the shape of the order-disorder transition line of the γ_1 and γ_2 phases. A short introduction to the respective methodologies is given in Sec. II. In Secs. III to V experimental aspects are treated, the results from diffuse scattering are presented, and the suggested metastable state Fe_3Pd with the $L1_2$ structure is addressed. In Sec. VI interaction parameters obtained from short-range-order scattering for states within the high-temperature γ solid solution are presented and compared with those from electronic-structure calculations at 0 K assuming the high-temperature paramagnetic state but also, for reference, the ferromagnetic state. Aspects of ordered structures and their stabilities are presented and discussed in Secs. VII and VIII.

II. METHODOLOGY

A. Basics of elastic diffuse scattering

Elastic diffuse scattering from an A-B alloy consists of contributions that originate from the presence of two elements (short-range-order scattering I_{SRO}) and from the static atomic displacements (size-effect scattering I_{SE} and Huang scattering I_{H}) [11,17–20]. Elastic diffuse scattering is expressed in Laue units (Lu), i.e., the scattering from a statistically uncorrelated arrangement (1 Lu per atom $= c_A c_B |f_A - f_B|^2$, where c_μ and f_μ are the composition and the atomic scattering factor of element $\mu = A,B$). The scattering contributions are separated by exploiting the various symmetries of the underlying Fourier series, the explicit dependence on the scattering vector $\mathbf{h} = (h_1,h_2,h_3)$ [scattering vector in reciprocal lattice units (rlu)], and—if x rays are employed—the different dependence of the atomic scattering factors of the elements on the scattering vector [21,22]. For a cubic binary alloy, short-range-order scattering is given by

$$I_{\mathrm{SRO}}(\mathbf{h}) = \sum_{lmn} \alpha_{lmn} \cos(\pi h_1 l) \cos(\pi h_2 m) \cos(\pi h_3 n), \quad (1)$$

where l,m,n are the indices of a neighboring shell in units of $a/2$ (a = lattice parameter) and α_{lmn} are the Warren-Cowley short-range-order parameters ($\alpha_{lmn} = 1 - \frac{P^{AB}_{lmn}}{c_B}$, where P^{AB}_{lmn} is the conditional probability that given an A atom at the origin, there will be a B atom in the neighboring shell lmn). For a binary cubic alloy, there are in total 25 such Fourier series when displacement scattering is considered up to quadratic terms; a detailed description is found in Refs. [11,17–20]. To separate SRO scattering from size-effect and Huang scattering, the approach of Georgopoulos and Cohen (GC) [22] was used.

B. First-principles calculations of effective cluster interactions

In this work, an Ising Hamiltonian was used for a statistical thermodynamic description of alloy energetics on a lattice, which presents the configurational energy of an alloy in terms of concentration-dependent effective cluster interactions

(ECIs):

$$H = \frac{1}{2}\sum_{p} V_p^{(2)} \sum_{i,j\in p} \delta c_i \delta c_j + \frac{1}{3}\sum_{t} V_t^{(3)} \sum_{i,j,k\in t} \delta c_i \delta c_j \delta c_k + \frac{1}{4}\sum_{q} V_q^{(4)} \sum_{ijk\ell\in q} \delta c_i \delta c_j \delta c_k \delta c_\ell . \quad (2)$$

Here, $V_s^{(n)}$ are the n-site ECI parameters for clusters of an s type; δc_i are the concentration fluctuations at sites i: $\delta c_i = c_i - c$, where c_i is the occupation number at site i, taking on values 1 or 0 if the site i is occupied by an Fe or Pd atom, respectively, and c is the concentration of Pd. The summation in (2) is carried out over all sites.

The ECI parameters for each concentration were obtained by the screened generalized perturbation method (SGPM) [23,24] implemented in the Green's function exact muffin-tin orbitals (EMTO) technique [25–27]. The coherent potential approximation (CPA) [28,29] was used in the EMTO calculations of random alloys. Screening parameters were determined in the 864-atom supercell calculations of random Fe-Pd with 37.5 at. % Pd, 50 at. % Pd, and 75 at. % Pd in both ferromagnetic and paramagnetic states using the locally self-consistent Green's function (LSGF) method [30]. The paramagnetic state was modeled by the disordered local moment (DLM) spin configuration [31,32].

The local density approximation (LDA) [33] was used for the exchange-correlation potential in the density functional theory (DFT) self-consistent calculations. All the EMTO-CPA calculations were performed using an orbital momentum cutoff of $l_{\max} = 3$ for partial waves. The integration over the Brillouin zone was performed using a $34 \times 34 \times 34$ grid of special $\mathbf{k}$ points determined according to the Monkhorst-Pack scheme [34]. In the case of ordered alloys, an equivalent grid of $\mathbf{k}$ points was used in the corresponding Brillouin zone.

To include the temperature-induced electronic excitations, the calculations were done using the Fermi function at 1000 K, which is close to the annealing temperatures in the experiment. Also high-temperature lattice constants of Fe-Pd alloys were used in order to take the thermal lattice expansion into consideration. They were determined from first-principles calculations using the Debye-Grüneisen model. In particular, the following lattice parameters were used: 3.819 Å, 3.849 Å, and 3.886 Å for Fe with 38.2, 50, and 81 at. % Pd, respectively.

III. EXPERIMENTAL

Iron and palladium, both with a purity of 99.95%, were purchased from Metalor SA (Neuchâtel, Switzerland) and from PRAXAIR MRC SA (Toulouse, France) to produce alloys with a nominal composition of Fe–38 at. % Pd and Fe–80 at. % Pd. The alloys were repeatedly remelted in an arc melter under an Ar atmosphere with a pressure of 300 mbar and swaged to rods with a diameter of about 1 cm. Single crystals were then grown by the Bridgman method.

Slices with a thickness of 3 mm and a diameter of 11 mm were cut by spark erosion. Their composition as determined by x-ray fluorescence analysis using standards gave a Pd concentration of 38.2(5) and 81.0(4) at. %. The samples were homogenized at 1373 K for 48 h and 24 h. Then the surface

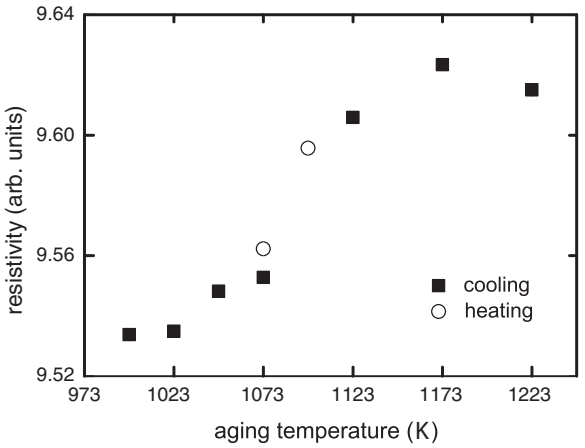

FIG. 2. Electrical resistance in cooling and heating runs for Fe–81 at. % Pd. Aging was done for 24 h; measurements were performed at liquid-nitrogen temperature.

of the samples was mechanically polished up to a grain size of 1 μm and 3 μm, respectively. Different treatments were applied subsequently.

The slice of Fe–38.2 at. % Pd was again homogenized for 2 d, then aged at 1023 K for 16 d and quenched into brine without breaking the quartz tube. According to Ref. [35] and data for Fe–50 at. % Pd, a relaxation time of ordering of at least 12 s is estimated. Thus, local atomic order and the quality of the surface are preserved in quenching.

The sample with Fe–81.0 at. % Pd was first electropolished for a few seconds at 7 V dc in a solution of 90 vol % methanol and 10 vol % hydrochloric acid to assure a single-crystalline surface. Subsequently no surface treatment was done as this step was found to lower the surface quality by producing Debye-Scherrer rings. The sample was aged at 1073 K for 14 d and quenched into brine without breaking the quartz tube. This heat treatment was chosen as preceding measurements of the electrical resistance had shown that a state of thermal equilibrium is then set up and quenched in. Those measurements were performed in heating and cooling runs, with the sample kept for 24 h at any selected aging temperature (Fig. 2). Within this isochronal program an equilibrium state is achieved in the linear regime (see, e.g., Pfeiler [36]) between 1050 and 1150 K.

To calculate thermal diffuse scattering and the total (thermal and static) Debye-Waller factor $\exp[-2B(\sin(\theta)/\lambda)^2]$, elastic constants were measured [37,38]. Cylinders with a ⟨110⟩ orientation were used for the pulse-echo-overlap method. From the resulting sound velocities the elastic constants were determined as $c_{11} = 189(2)$ GPa, $c_{12} = 158(2)$ GPa, $c_{44} = 79.8(9)$ GPa for Fe–38 at. % Pd and $c_{11} = 226(2)$ GPa, $c_{12} = 161(2)$ GPa, $c_{44} = 90.6(6)$ GPa for Fe–80 at. % Pd. Because of the different values for the change of lattice parameter with composition that enter the determination of the static Debye-Waller factor, the values of B differ being 0.680 Å^2 for Fe–38 at. % Pd and 0.371 Å^2 for Fe–81 at. % Pd.

The diffuse scattering experiments were done with Mo Kα radiation that is generated by a 12 kW Rigaku rotating anode (for the setup, see Yu *et al.* [39]). The diffuse intensities were measured on a three-dimensional cubic mesh of 0.1 reciprocal

lattice units (rlu) at positions within 1.5 to 7 rlu. Each measurement comprised about 12000 positions in reciprocal space. Scattering was calibrated using polystyrene. To obtain the elastic diffuse scattering, the inelastic scattering contributions of Compton scattering and thermal diffuse scattering up to third order were calculated and subtracted from the calibrated x-ray intensities. Tabulated values for the atomic scattering factors and Compton scattering were employed [40].

IV. DIFFUSE SCATTERING

The calibrated diffuse x-ray scattering within the (100) plane is shown in Fig. 3. The patterns of the total (elastic and inelastic) scattering for both alloys show diffuse maxima close to the X position. This feature is expected for local order when $L1_2$ and $L1_0$ ordered structures are located nearby in the phase diagram. The missing 030 maximum with Fe–81.0 at. % Pd and the shift off this position for Fe–38.2 at. % Pd

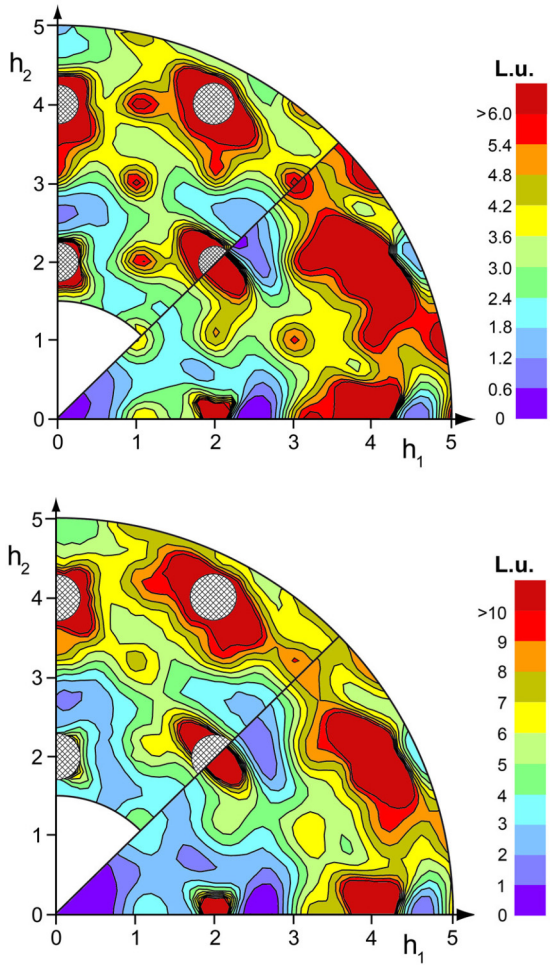

FIG. 3. (Color online) Contour plot of diffuse scattering for the (100) plane from Fe–38.2 at. % Pd at 1023 K (top) and Fe–81.0 at. % Pd at 1073 K (bottom). In the upper triangles the measured data are shown in the range of 1.5–5.0 rlu. The regions around Bragg reflections that were not used in data evaluation are hatched. In the lower triangles the recalculated diffuse scattering (using the SRO parameters and static atomic displacements of Tables I and II as well as the thermal diffuse scattering and Compton scattering) are shown.

immediately indicate that linear displacement scattering is not negligible with respect to short-range-order scattering.

The separated SRO scattering was fitted using the Warren-Cowley SRO parameters α_{lmn}. The number of parameters to be considered was selected according to the R value of the fit, their relevance was judged by a comparison with their standard deviations, and finally the separated and recalculated SRO scattering was compared. To consider also the regions around Bragg reflections (strong thermal diffuse scattering prohibits excellent data separation within 0.2 rlu around these positions), SRO scattering was smoothly extrapolated in these regions using values of 0.6 Lu and 0.3 Lu for Fe–38.2 at. % Pd and Fe–81.0 at. % Pd, respectively. 21 SRO parameters α_{lmn} were selected (Table I); the separated and recalculated scattering is shown in Fig. 4.

The sign sequence of $L1_2$ or $L1_0$ type of local order is well resolved for the nearby shells, expectedly better for Fe–38.2 at. % Pd that exhibits a somewhat stronger diffuse maximum at X positions than Fe–81.0 at. % Pd (4.0 Lu versus 3.0 Lu). For both data sets, the magnitude of α_{000} that has to be 1 by theory is not within one standard deviation (uncertainty is solely based on counting statistics). The value is slightly larger than 1 as repeatedly seen with diffuse x-ray scattering. The reason for such an outcome is not known.

To recalculate the diffuse scattering patterns of Fig. 3, also the separated size-effect scattering was fitted, using species-dependent static atomic displacement parameters. The parameter sets are shown in Table II. In the case of Fe–81.0 at. % Pd, the displacements between minority atoms are larger than those between majority atoms that mainly determine the average (gray) lattice. For Fe–38.2 at. % Pd, the displacement parameters between Pd-Pd pairs and Fe-Fe pairs are of the same order of magnitude. The scattering contributions that comprise short-range-order scattering and size-effect scattering, as well as Compton scattering and thermal diffuse scattering, are also shown in Fig. 3. The modulation in diffuse scattering in general, and also around 030, is reproduced. Note that slightly lower values will arise in the recalculated scattering as higher-order elastic and inelastic displacement scattering are not included.

V. TYPE OF LOCAL ORDER FOR Fe–38.2 at. % Pd

Typical features of local order may serve as an indicator for long-range-ordered structures that are under discussion. For short-range-ordered Fe–38.2 at. % Pd these are the ordered structures $L1_2$ and $L1_0$. As composition is fixed in ordering, the case of maximum degree of long-range order that is compatible with $c_{\mathrm{Pd}} = 0.382$ [$\eta = \frac{4}{3}(1 - c_{\mathrm{Pd}})$ for $L1_2$ and $\eta = 2c_{\mathrm{Pd}}$ for $L1_0$] was considered. Tendencies for ordering are then revealed when a random arrangement is taken as reference; nearest-neighbor configurations give detailed information. Such crystals were modeled and the case of Pd nearest neighbors around Fe atoms was considered for which the $L1_2$ and $L1_0$ structures exclusively have the Clapp configurations C16 and C129, respectively (for the nomenclature of the nearest-neighbor configurations, see Clapp [41]). Table III summarizes the configurations that are largest enhanced over those of a random arrangement. One notices that the configuration largest enhanced in the

TABLE I. Warren-Cowley short-range-order parameters α_{lmn} as determined for Fe–38.2 at. % Pd at 1023 K and Fe–81.0 at. % Pd at 1073 K. For comparison, the data set of Ref. [12] for Fe–50 at. % Pd at 1020 K is shown. Data from diffuse scattering and from first-principles DLM calculations are given. Furthermore, the signs of α_{lmn} for $L1_2$ and $L1_0$ are provided.

	α_{lmn}						
	Fe–38.2 at. % Pd		Fe–50 at. % Pd		Fe–81.0 at. % Pd		
lmn	Scattering	DLM	Scattering (Ref. [12])	DLM	Scattering	DLM	$L1_2$, $L1_0$
000	1.2570(111)	1	1	1	1.1288(132)	1	
110	−0.1059(54)	−0.1002	0.0019(37)	−0.1108	−0.1182(66)	−0.1259	−
200	0.1483(52)	0.1059	0.1399(56)	0.1195	0.1299(55)	0.1095	+
211	−0.0233(31)	−0.0099	−0.0079(22)	−0.0096	−0.0001(35)	−0.0004	−
220	0.0291(34)	0.0405	0.0379(30)	0.0463	0.0470(33)	0.0393	+
310	−0.0093(23)	−0.0161	−0.0225(23)	−0.0199	−0.0202(27)	−0.0188	−
222	0.0218(33)	0.0212	0.0295(30)	0.0256	0.0172(36)	0.0190	+
321	−0.0050(14)	−0.0069	−0.0127(16)	−0.0089	−0.0021(15)	−0.0082	−
400	0.0295(38)	0.0152	0.0244(45)	0.0185	−0.0168(42)	0.0125	+
330	−0.0029(25)	−0.0002	−0.0030(27)	0.0004	0.0063(29)	0.0040	−
411	−0.0036(21)	−0.0001	−0.0135(19)	0.0011	−0.0029(23)	0.0054	−
420	0.0046(21)	0.0082	0.0135(22)	0.0103	−0.0018(20)	0.0042	+
233	−0.0013(20)	−0.0021	−0.0081(19)	−0.0027	0.0007(23)	−0.0014	−
422	0.0029(20)	0.0057	0.0138(18)	0.0075	0.0011(20)	0.0027	+
431	−0.0028(14)	−0.0018	−0.0096(13)	−0.0023	0.0003(16)	0.0001	−
510	0.0004(23)	−0.0030		−0.0042	−0.0028(24)	−0.0036	−
521	0.0006(14)	−0.0017		−0.0025	−0.0031(15)	−0.0015	−
440	−0.0036(25)	0.0024		0.0030	0.0077(27)	−0.0026	+
433	−0.0012(19)	−0.0009		−0.0012	−0.0016(24)	0.0005	−
530	0.0022(18)	−0.0004		−0.0005	0.0071(20)	0.0005	−
244	0.0026(19)			0.0029	−0.0054(19)	−0.0007	+
600	0.0123(35)	0.0028		0.0038	−0.0172(39)	0.0021	+

SRO state, C16, is also the dominant configuration with nonstoichiometric $L1_2$. However, the configurations where one Pd atom is added (C34 with $L1_2$) or subtracted (C111 with $L1_0$) to consider nonstoichiometry are both on the list for well-enhanced Clapp configurations in the SRO state. Thus, no decision on the type of local order seems possible.

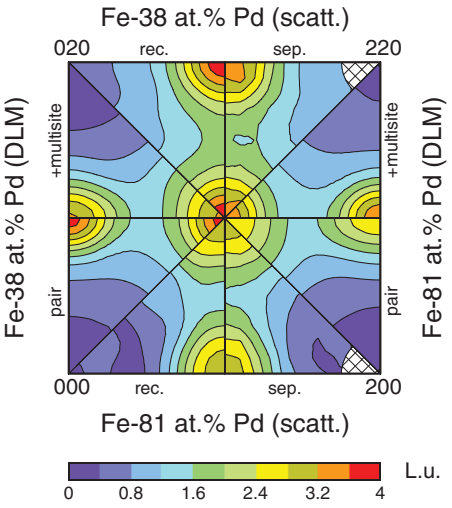

FIG. 4. (Color online) Separated and recalculated (parameters from Table I) SRO scattering from Fe–38.2 at. % Pd at 1023 K and Fe–81.0 at. % Pd at 1073 K. Also shown is the SRO scattering using DLM calculations excluding and also including many-body interactions.

In the literature, Fe_3Pd ($L1_2$) is discussed as metastable state during long-term aging at sufficiently low temperatures. Such investigations are currently under way. One may already note that aging of short-range-ordered Fe–38 at. % Pd for 14 weeks at 350 °C (i.e., within the α-γ_1 two-phase regime) does not lead to a tetragonal splitting of the $h00$ Bragg reflections while the long-range-order parameter increases to $\sim 0.19(4)$ (full ordering in the $L1_2$ structure gives 0.82 for the given composition). A splitting would indicate the formation of an $L1_0$-type structure. Longer aging times and different aging

TABLE II. Static atomic displacements $\langle x^{\mu\mu}_{lmn} \rangle$ in units of the lattice parameter a for Fe–38.2 at. % Pd at 1023 K and Fe–81.0 at. % Pd at 1073 K.

	Fe–38.2 at. % Pd		Fe–81.0 at. % Pd	
lmn	$\langle x^{\mathrm{PdPd}}_{lmn} \rangle$	$\langle x^{\mathrm{FeFe}}_{lmn} \rangle$	$\langle x^{\mathrm{PdPd}}_{lmn} \rangle$	$\langle x^{\mathrm{FeFe}}_{lmn} \rangle$
110	0.00744(6)	−0.00369(4)	0.00010(1)	−0.1172(6)
200	−0.00466(21)	0.00028(18)	0.00139(5)	0.0674(13)
211	0.00114(6)	0.00023(6)	0.00033(1)	0.0101(3)
121	0.00185(5)	−0.00033(3)	0.00037(1)	0.0056(2)
220	0.00012(8)	−0.00086(7)	−0.00012(2)	0.0019(7)
310	−0.00023(6)	−0.00021(4)	−0.00011(1)	−0.0077(4)
130	−0.00195(7)	−0.00114(5)	0.00041(1)	0.0164(6)
222	−0.00009(6)	−0.00054(5)	0.00004(1)	0.0030(3)
321	0.00110(4)	0.00003(3)	−0.00005(1)	0.0018(2)
231	−0.00044(3)	−0.00002(3)	0.00009(1)	0.0039(2)

TABLE III. Enhancement factor (if >4) over a random arrangement and abundance within the nearest-neighbor spectrum for short-range-ordered Fe–38.2 at. % Pd. For comparison the enhancement factors (again over a random arrangement) of nonstoichiometric $L1_2$ and $L1_0$ with $c_{Pd} = 0.382$ are shown. For the nomenclature of the Clapp configurations, see Ref. [41]. The case of Pd atoms around Fe atoms is considered.

Clapp	Enhancement factor			Abundance
configuration	$L1_2$	SRO	$L1_0$	in %
C 16	179	9.1	60	1.04
C 34	45	4.9		3.82
C 58	21	7.2	19	1.34
C 59	16	6.1	16	1.39
C 60	24	4.1	21	0.69
C 111	7	6.4	100	1.47
C 129		5.6	293	0.18

temperatures are required to judge whether there is such a metastable $L1_2$ state.

VI. EFFECTIVE INTERACTION PARAMETERS

A. EPI parameters from diffuse scattering

The SRO parameters of Table I and the inverse Monte Carlo (IMC) method [42] were used to determine the effective pair interaction (EPI) parameters V_{lmn} of an Ising Hamiltonian, $V_{lmn} = V_{lmn}^{AA} + V_{lmn}^{BB} - 2V_{lmn}^{AB}$, which are connected to the ordering energy per atom by

$$E_{\mathrm{ord}}/N = \frac{1}{2} c_A c_B \sum_{lmn} V_{lmn} \alpha_{lmn}. \tag{3}$$

Crystals with $48 \times 48 \times 48$ atoms and linear boundary conditions were employed. An average over ten crystals all compatible with the SRO parameters and their standard deviations (Table I) were used to propagate the uncertainty of the experimental SRO parameters. A set of 20 EPI parameters with Fe–81 at. % Pd and 16 parameters with Fe–38.2 at. % Pd were sufficient to reproduce the SRO parameters and the SRO scattering by subsequent Monte Carlo (MC) simulations. The values are given in Table IV.

Table IV also shows EPI parameters for Fe–50 at. % Pd based on the SRO parameters of Ref. [12]. Here, a data set with 14 EPI parameters was considered best suited to reproduce the SRO parameters in subsequent MC simulations; the same crystal size and the same boundary conditions as for the other two alloys were employed. These data and those given by Mehaddene [13] typically agree only within ~1 meV.

A strong concentration dependence of the EPI parameters is observed, best seen with V_{110}. There is, however, no steady decrease or increase with composition; whereas V_{110} is dominant and positive for the Fe-rich and Pd-rich alloys, V_{110} is close to zero and even slightly negative at equiatomic composition. In that case there is still local order as diffuse maxima at 100 positions are present.

TABLE IV. EPI parameters V_{lmn} as determined by the inverse Monte Carlo method using the Warren-Cowley short-range-order parameters of Table I and of Fe–50 at. % Pd at 1020 K from Ref. [12].

	V_{lmn} (meV)					
	Fe–38.2 at. % Pd		Fe–50 at. % Pd		Fe–81.0 at. % Pd	
lmn	Scattering	DLM	Scattering	DLM	Scattering	DLM
110	59.2(27)	51.2	−3.5(4)	63.1	121.4(63)	156.0
200	−37.7(31)	−24.7	−46.4(18)	−15.9	−26.8(37)	7.7
211	11.5(15)	5.5	0.4(3)	6.4	−11.0(26)	17.7
220	18.2(27)	−0.4	4.6(12)	0.5	−21.1(29)	5.6
310	−5.6(20)	0.9	6.5(3)	0.9	1.2(23)	2.3
222	−3.1(21)	−0.5	−4.6(6)	−1.0	−22.4(33)	−0.3
321	3.3(19)	0.8	1.0(2)	0.9	−13.7(20)	2.1
400	−9.1(39)	0.4	0.6(10)	0.4	40.5(30)	−0.0
330	6.2(26)	−1.8	−3.3(5)	−2.7	−16.8(22)	−5.2
411	−3.4(16)	0.3	1.9(2)	0.1	15.4(16)	−0.2
420	0.3(19)	0.3	0.3(3)	0.1	5.8(16)	0.2
233	0.2(15)	0.2	1.8(4)	−0.0	−6.9(19)	0.3
422	1.7(14)	0.3	−0.5(2)	0.2	−3.6(10)	0.7
431	2.0(7)	0.2	1.3(2)	−0.0	−4.2(9)	−0.4
510	−2.3(14)	0.2			15.2(15)	−0.1
521	−0.5(3)	0.1			4.4(8)	−0.1
440					−9.7(9)	0.5
433					1.3(15)	−0.2
530					−2.8(7)	0.1
244					4.6(9)	0.4

B. ECI parameters from electronic-structure calculations

In Fig. 5, the effective pair interactions $V_p^{(2)}$ are shown for the three alloy compositions that were investigated by diffuse scattering. One notices that the data for the FM and DLM states differ only slightly. Still, as will be shown below, this difference, together with the three- and four-site interactions, is sufficient to produce a substantial change in the value of any order-disorder transition temperature.

For a series of compositions, values of $V_p^{(2)}$ of the first two neighboring shells are shown in Fig. 6. A smooth increase of $V_p^{(2)}$ with increasing Pd fraction is seen for both shells, being stronger for larger Pd fractions. Although the tendency for order is increasing at both coordination shells, the switch from negative to positive values of $V_{200}^{(2)}$ means that the tendency for $L1_2$ type of order decreases, which is probably the reason for the appearance of a large variety of ground-state structures in Pd-rich alloys [5,6].

Multisite interactions in Fe-Pd also exhibit quite a strong dependence on concentration. Besides, they appear to be much more sensitive to the magnetic state than pair interactions. This is seen in Table V where the three strongest (on average) three- and four-site interaction parameters are shown in the FM and DLM states, again for the same alloy compositions as investigated in the diffuse scattering experiment. An interesting feature of the Fe-Pd system is the fact that four-site interaction parameters in the DLM state are substantially stronger than those in the FM state. At the same time, three-site interaction parameters are stronger in the FM state. As will be shown below, multisite interactions strongly affect the state of order in Fe-Pd.

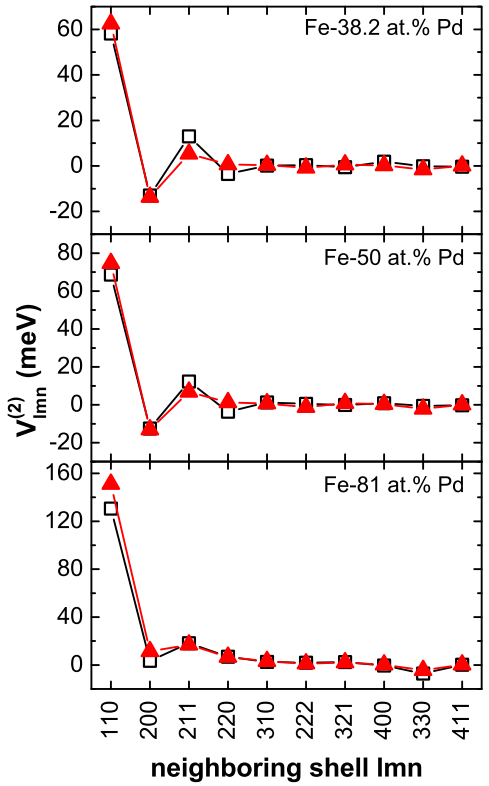

FIG. 5. (Color online) Effective pair interactions $V_p^{(2)}$ in Fe-Pd alloys for three different compositions in the DLM (triangles) and FM (squares) states.

To compare the results from the electronic-structure calculations with those from diffuse scattering, Warren-Cowley short-range-order parameters α_{lmn} were determined by Monte Carlo simulations (Table I). A close agreement with the values from diffuse scattering is noted in general, also in SRO scattering (Fig. 4). Deviations at larger neighboring shells (of the order of 4 standard deviations) are presumably connected to counting statistics. The large discrepancy with α_{110} of Fe–50 at. % Pd, where an exceptionally small value close to 0 was found in Ref. [12], does not allow for such an explanation.

Based on these Warren-Cowley short-range-order parameters, EPI parameters V_{lmn} were determined by the IMC method.

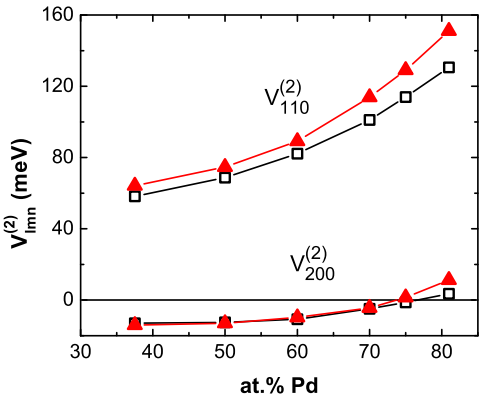

FIG. 6. (Color online) Concentration dependence of the effective pair interactions $V_p^{(2)}$ at the first two coordination shells in the DLM (triangles) and FM (squares) states.

TABLE V. Strongest three- and four-site interaction parameters in Fe-Pd for FM and DLM states and various alloy compositions. In the case of three-site interactions, 111, 112, and 114 clusters correspond to the triangles formed by three nearest neighbors, two nearest-neighbor pairs and one pair of the next-nearest neighbors, and two nearest neighbors and one pair of fourth-nearest neighbors, respectively. In the case of four-site interactions, *tnn* is the tetrahedron of nearest neighbors, *tnnn* the tetrahedron with one pair of next-nearest neighbor atoms, and *cpd* the cluster formed by four consecutive atoms in close-packed direction.

	V_t^3 and V_q^4 (meV)					
	Fe–38.2 at. % Pd		Fe–50 at. % Pd		Fe–81 at. % Pd	
Type	FM	DLM	FM	DLM	FM	DLM
$V^{(3)}_{111}$	40.0	14.1	38.4	14.8	29.1	7.5
$V^{(3)}_{112}$	−14.8	−2.4	−12.5	−2.0	−4.1	8.0
$V^{(3)}_{114}$	−4.1	6.5	8.0	8.0	40.9	24.1
$V^{(4)}_{tnn}$	11.0	19.0	5.8	13.2	−1.1	7.1
$V^{(4)}_{tnnn}$	10.9	26.5	10.2	25.7	−0.8	−0.8
$V^{(4)}_{cpd}$	−3.8	17.7	−5.0	22.0	4.8	42.0

They are given in Table IV. In contrast to the result from diffuse scattering, the leading nearest-neighbor interaction parameter V_{110} as obtained from first-principles calculations shows a systematic dependence on composition: it increases with increasing Pd fraction. This point needs further clarification.

VII. ORDER-DISORDER TRANSITIONS

A. Pd-rich side of the phase diagram from diffuse scattering

Order-disorder transition temperatures on the Pd-rich side of the phase diagram were determined by canonical MC simulations. As starting crystals either those with a random arrangement or a maximum degree of long-range order of the $L1_0$ or $L1_2$ type that is compatible with the given composition were chosen. Whereas antiphase boundaries will arise in the ordered state if the starting crystal shows a random arrangement, this situation is avoided when the crystal is long-range ordered. When the type of the starting crystal is changed, transition temperatures vary typically within ±5 °C. If one employs EPI parameters independent of composition according to Table IV [those of Fe–50 (and 81) at. % Pd for the γ_1 (and γ_2) phase], the order-disorder transition line is not reproduced [Fig. 1(a)].

Next, parameter sets of V_{lmn} were employed that were determined by linear interpolation between values from Fe–50 at. % Pd and Fe–81 at. % Pd as provided in Table IV. To decide whether an alloy with a given composition belongs to the γ_1 phase (with $L1_0$ type of structure) or to the γ_2 phase (with $L1_2$), ordering energies per atom were determined. It turned out that the $L1_0$ phase was stable up to ∼63.5 at. % Pd and the $L1_2$ phase at higher Pd fractions for both EPI parameter sets. This value is close to the γ_1-γ_2 two-phase region of 60.5 to 62.5 at. % Pd given by Okamoto [1].

In Fig. 1(a) the EPI parameters from diffuse scattering were employed to determine order-disorder transition temperatures. The figure shows that the highest order-disorder transition temperatures are no longer observed at the stoichiometries

of the $L1_0$ and $L1_2$ structures. Instead, there is an increase towards a temperature range between Fe–(∼55 to ∼65) at. % Pd. No individual maxima for the γ_1 and γ_2 phases are resolved. Two points should be considered: (i) The experimental phase diagram data as compiled by Okamoto [1] are strongly scattered; individual maxima of the γ_1 and γ_2 phases as found in Refs. [7,8] were not always resolved in experiments (see, e.g., Ref. [43]). (ii) Deviations from the strictly linear dependence of the EPI parameters on composition will modulate the order-disorder line (see the transition lines around Fe–50 at. % Pd and Fe–75 at. % Pd where concentration-independent EPI parameter sets were employed). One notices that the shape of the order-disorder line as a function of composition is largely reproduced by the MC simulations. There remains one obvious difference: the transition temperatures are lower by about 100 °C compared to the experimental values. One reason for this underestimate might be the tetragonality in the γ_1 phase. An increased stability of the $L1_0$ phase due to tetragonality was mentioned by Mohri *et al*. [9].

As stated above, the EPI parameters as obtained by Mehaddene [13] were not employed, but those based on a recalculation from the published short-range order parameters (see Table IV). The differences between both parameter sets turned out to be sufficient to raise the order-disorder transition temperature of FePd ($L1_0$) from 705 K to 870 K.

B. Atomic ordering from first-principles calculations

Effective interactions from first-principles calculations were also used in order to determine order-disorder transition temperatures. In Fig. 1(b), results for transition temperatures on the Pd-rich side are shown using FM and DLM effective interactions as obtained by the SGPM. Note that any contribution from strain-induced interactions, lattice vibrations, and electronic and magnetic excitations (apart from the use of the DLM model for the paramagnetic state) are neglected. The strain-induced interactions are expected to be small in this system since Fe atoms are in the high-spin state (close to $3\mu_B$ for lattice parameters at ambient conditions). This can be clearly seen in the first-principles calculations of random alloys that show very small charge transfer effects between Fe and Pd atoms. The effect of lattice vibrations and electronic excitations is not known, but is not believed to be dominant.

As for the magnetic excitations, a rough estimate can be given by comparing the results in the FM and DLM states. Although alloys are in a paramagnetic state above the order-disorder transition temperature, the ECI parameters can be substantially affected by magnetic short-range order. Thus, in the cases where the magnetic transition is close to the atomic ordering transition, the magnetic excitations should move the ordering transition temperature from the DLM results towards the FM ones. An accurate account of all the possible effects is beyond the scope of this work.

Nevertheless, the results obtained using only the chemical contribution to the effective interactions provide an interesting qualitative picture. First of all, although FM and DLM $V_p^{(2)}$ look very similar, there is a difference of up to 150 K between the corresponding transition temperatures. Another interesting result is the fact that the 3- and 4-site interactions accentuate the maxima in ordering temperatures as already indicated when the $V_p^{(2)}$ data were used; for the FM data the maximum tends towards the γ_1 state, for the DLM data towards the γ_2 state. This means that the observed shape of the transition line is driven by multisite interactions and occurs especially in the range of compositions where the transition temperature reaches its maximum value.

VIII. DISCUSSION

A. Effect of magnetism on atomic ordering and effective interactions

According to the first-principles results by Barabash *et al*. [5] and Chepulskii *et al*. [6], the experimentally observed $L1_2$ structure in $FePd_3$ is not stable, at least at 0 K in the FM state. In particular, the DO_{23} structure is more stable than $L1_2$ by about 3 meV (see Table VI of Ref. [6]). Although the present FM SGPM ECI parameters do not reproduce this result ($L1_2$ is more stable than DO_{23} by about 2 meV), the direct total energy calculations confirm the result of Chepulskii *et al*. [6]. On the other hand, the situation gets reversed in the DLM state: The $L1_2$ structure is more stable than DO_{23} by a similar marginal amount of energy of about 2 meV in the direct total energy calculations as well as in the ordering energy calculations using the DLM SGPM ECI parameters.

The failure of the SGPM to predict the correct ordered structure of $FePd_3$ in the FM state (although the error is very small) can be attributed to different approximations connected with the SGPM. Nevertheless, there is one important issue: the Ising model given by Eq. (2) can be deficient in magnetic alloys due to a dependence of the chemical interactions between atoms upon their local environment, which affects the local magnetic state of interacting atoms [44,45]. This is the case for $3d$-metal alloys since the bonding and magnetism are directly interconnected simply through the filling of the d band.

In order to demonstrate that this is also the case for Fe-Pd alloys, calculations of the nearest-neighbor effective interactions in Fe–50 at. % Pd in the FM state were performed using a 256-atom supercell with randomly distributed Fe and Pd atoms. This is a realistic model of an alloy, where fluctuations of the local composition are present leading to differences among all Fe and all Pd atoms, for instance, due to a difference in their local magnetic moments. The electronic structure of such a supercell and the nearest-neighbor EPIs, $V_{110}^{(2)}$, for different pairs of Fe and Pd atoms have been determined by the LSGF method.

In Fig. 7 it is shown how $V_{110}^{(2)}$ depends on the number of nearest neighbors of Pd and Fe atoms involved in the corresponding interaction. If the Ising model were valid in this system in the FM state, there would be no dependence of the interactions on the local environment: ECI parameters of the Ising model do not depend on the local environment of individual atoms, but on the alloy configuration on average. This is not the case in the FM Fe-Pd alloys: While effective interactions are not sensitive to the local environment of Pd atoms, they change substantially when the number of Fe nearest neighbors of Fe atoms is varied.

In Fe-Pd one can see the deficiency of the Ising model via the ordering effects in the first coordination shell. Here, a reduction of the number of Fe nearest neighbors of Fe atoms

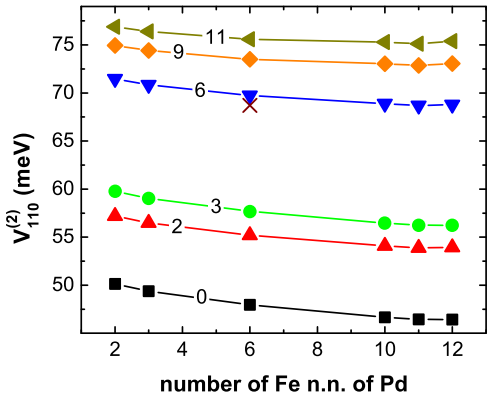

FIG. 7. (Color online) Local effective pair interactions $V_{110}^{(2)}$ for Fe-Pd nearest-neighbor pairs of Fe–50 at. % Pd in the FM state. The numbers on the lines indicate the numbers of Fe nearest neighbors (n.n.) of Fe. Also given is the value in CPA calculation (cross).

and a simultaneous increase of the number of Fe atoms next to Pd should lead to a reduction of the nearest-neighbor $V_p^{(2)}$ (Fig. 7). However, when $V_{110}^{(2)}$ is obtained in a homogeneous model of a random alloy, the simulation works quite well as all Fe and Pd atoms are equivalent to each other (CPA). That means that the Ising model and SGPM can still make sense in the FM state, but only for the description of weak ordering effects in random alloys. In contrast, in the DLM state, the effect of the local environment on $V_{110}^{(2)}$ is very small, which makes the theoretical modeling of atomic ordering in the paramagnetic state described above valid.

It is clear that the usual cluster expansion of *enthalpies of formation* can easily fail for Fe-Pd alloys in the FM state in general, but it can still predict possible ground-state structures at 0 K, if a large set of ordered structures is used. As an example, the presence of the suggested phase Fe_3Pd_9 with an order-disorder transition temperature around 800 K [6] is not confirmed in the present calculations. Monte Carlo simulations done with the EPI parameters from diffuse scattering showed that states above the Curie temperature up to 800 K are unstable with respect to the formation of the $L1_2$ structure. Similar results are obtained in Monte Carlo simulations with the DLM SGPM ECI parameters for Fe–75 at. % Pd, where a transition to the $L1_2$ structure is observed. Also, an analysis of nearest-neighbor configurations does not reveal the same dominant configuration as in the diffuse scattering from Fe–81 at. % Pd.

B. Phase stability

In Fig. 1(b) the ECI parameters from first-principles calculations in the FM and DLM states were employed to determine order-disorder transition temperatures. For comparison the result from Chepulskii *et al.* [6] obtained with their pair and many-body interaction parameters is also shown in Fig. 1(b). A drastic difference is obvious: their transition temperatures are lower by about 400 K in the range of the γ_1 phase and by about 200 K in the range of the γ_2 phase. Although the strong decrease of the transition line for Fe-Pd alloys with less than ~65 at. % Pd coincides with the strong increase of the Curie temperature with composition in this range, it is most probably just the effect of the strong concentration dependence of the effective interactions (especially multisite) in this region since it is observed in both ferromagnetic and paramagnetic states.

If one performs MC simulations with the present ECI parameters in the DLM and FM states, the lower enthalpy of formation in the FM state (by 9.8 meV) stabilizes the ordered $L1_0$ structure and leads to a higher order-disorder temperature of 1060 K in comparison with 800 K if the paramagnetic state were present. The experimental value for FePd is about 950 K. Thus, values from phase diagram, diffuse scattering, and present first-principles calculations are close to one another. A stabilization of an ordered phase due to ferromagnetism was recently demonstrated by Rahaman *et al.* [46] using first-principles calculations. This study for Fe-Co showed that the order-disorder transition temperatures increase with magnetic order.

There is a large difference in the transition temperatures between the two first-principles calculations in the FM model. The reason for the discrepancy between the two studies is believed to be related to the type of cluster expansion. As has been demonstrated above, the ECI parameters in Fe-Pd are not only strongly concentration dependent; they depend on the local environment of the interacting atoms; i.e., they are *configurationally* dependent. The concentration-independent cluster expansion of the enthalpies of formation of the ordered structures in this case is just a brute force method providing a representation of the enthalpies of formation in terms of the corresponding ECIs. These ECIs, however, have very little in common with the concentration-dependent ECIs, which represent the expansion of the configurational energy, or generally speaking the response of a random system to a specific configurational perturbation. Thus, one set of interactions cannot be reduced to the other in Fe-Pd [47]. As for the statistical thermodynamic simulations of atomic ordering at a fixed alloy composition, it is important not simply to reproduce the corresponding ordering energies. Correct values of interactions are required, which *uniquely* determine experimentally measurable atomic correlation functions [48] and finally the transition temperatures [49].

IX. CONCLUSION

Diffuse scattering and electronic-structure calculations were employed to determine interaction parameters and to address the phase stability of Fe-Pd alloys.

(1) The first-principles calculations demonstrate that the magnetic state has to be considered in determining interaction parameters; the ECI parameters in FM or DLM states are different and thus change the phase stability.

(2) A strong dependence of the effective interaction parameters on composition is found. If this concentration dependence is considered, it is possible to reproduce the characteristics of the order-disorder transition temperature of the γ_1 and γ_2 phases, i.e., the strong shifts of congruent ordering off the respective stoichiometry. The first-principles calculations reveal that many-body interactions play a decisive role herewith.

(3) FePd and $FePd_3$ with $L1_0$ and $L1_2$ structure, respectively, are found as stable structures at elevated temperatures, consistent with experimental findings. No support is reached for Fe_3Pd_9 above the Curie temperature.

(4) Differences in outcome from previous *ab initio* calculations may originate from the approximations then employed to determine the enthalpy of formation of a complex system like Fe-Pd with atomic and magnetic order.

ACKNOWLEDGMENTS

The authors are grateful to E. Fischer for his support in growing the single crystals. They also thank J. Löffler for his support and encouragement. This work was partially supported by the "Schweizerischer Nationalfonds zur Förderung der wissenschaftlichen Forschung". A.V.R. is grateful to the Swedish Research Council (VR Project No. 15339-91505-33). Part of this work was performed within the VINN Excellence Center Hero-m, financed by VINNOVA, the Swedish Government Agency of Innovation Systems, Swedish Industry, and the Royal Institute of Technology. The computations were partly performed on resources provided by the Swedish National Infrastructure for Computing (SNIC) at the National Supercomputer Center (NSC) in Linköping, Sweden.

[1] H. Okamoto, *Phase Diagrams of Binary Iron Alloys* (ASM International, Materials Park, OH, 1993).
[2] R. Hultgren, P. D. Desai, D. T. Hawkins, M. Gleiser, and K. K. Kelly, *Selected Values of the Thermodynamic Properties of Binary Alloys* (ASM, Metals Park, OH, 1973).
[3] K. H. J. Buschow, P. G. van Engen, and R. Jongebreur, J. Magn. Magn. Mater. **38**, 1 (1983).
[4] S. Kang, Z. Jia, D. E. Nikles, and J. W. Harrell, J. Appl. Phys. **95**, 6744 (2004).
[5] S. V. Barabash, R. V. Chepulskii, V. Blum, and A. Zunger, Phys. Rev. B **80**, 220201(R) (2009).
[6] R. V. Chepulskii, S. V. Barabash, and A. Zunger, Phys. Rev. B **85**, 144201 (2012).
[7] E. Raub, H. Beeskow, and O. Loebich, Jr., Zeitschrift für Metallkunde **54**, 549 (1963).
[8] T. Takezawa, T. Miwa, and T. Yokoyama, J. Jpn. Inst. Met. **51**, 285 (1987).
[9] T. Mohri, T. Horiuchi, H. Uzawa, M. Ibaragi, M. Igarashi, and F. Abe, J. Alloys Compd. **317-318**, 13 (2001).
[10] T. Mohri and Y. Chen, J. Alloys Compd. **383**, 23 (2004).
[11] B. Schönfeld, Prog. Mater. Sci. **44**, 435 (1999).
[12] T. Mehaddene, J. M. Sanchez, R. Caudron, M. Zemirli, and V. Pierron-Bohnes, Eur. Phys. J. B **41**, 207 (2004).
[13] T. Mehaddene, J. Phys.: Condens. Matter **17**, 485 (2005).
[14] R. Hultgren and C. A. Zapffe, Zeitschrift für Kristallographie **99**, 509 (1938).
[15] M. Engelke and B. Schönfeld, Acta Mater. **61**, 5087 (2013).
[16] M. Sugiyama, R. Oshima, and F. E. Fujita, Trans. JIM **27**, 719 (1986).
[17] G. Kostorz, in *Physical Metallurgy*, edited by R. W. Cahn and P. Haasen (North-Holland, Amsterdam, 1996), p. 1115.
[18] W. Schweika, *Disordered Alloys: Diffuse Scattering and Monte Carlo Simulation*, Springer Tracts in Modern Physics No. 141 (Berlin, Springer, 1998).
[19] G. E. Ice and C. J. Sparks, Annu. Rev. Mater. Sci. **29**, 25 (1999).
[20] V. M. Nield and D. A. Keen, *Diffuse Neutron Scattering from Crystalline Materials* (Oxford, Clarendon, 2001).
[21] B. Borie and C. J. Sparks Jr., Acta Crystallogr. A **27**, 198 (1971).
[22] P. Georgopoulos and J. B. Cohen, J. Phys. (Paris) Colloq. **38**, C7 (1977).
[23] A. V. Ruban and H. L. Skriver, Phys. Rev. B **66**, 024201 (2002); A. V. Ruban, S. I. Simak, P. A. Korzhavyi, and H. L. Skriver, *ibid.* **66**, 024202 (2002).
[24] A. V. Ruban, S. Shallcross, S. I. Simak, and H. L. Skriver, Phys. Rev. B **70**, 125115 (2004).
[25] L. Vitos, H. L. Skriver, B. Johansson, and J. Kollár, Comput. Mater. Sci. **18**, 24 (2000).
[26] L. Vitos, Phys. Rev. B **64**, 014107 (2001).
[27] L. Vitos, I. A. Abrikosov, and B. Johansson, Phys. Rev. Lett. **87**, 156401 (2001).
[28] B. L. Gyorffy, Phys. Rev. B **5**, 2382 (1972).
[29] P. Soven, Phys. Rev. **156**, 809 (1967).
[30] O. E. Peil, A. V. Ruban, and B. Johansson, Phys. Rev. B **85**, 165140 (2012); I. A. Abrikosov, A. M. N. Niklasson, S. I. Simak, B. Johansson, A. V. Ruban, and H. L. Skriver, Phys. Rev. Lett. **76**, 4203 (1996); I. A. Abrikosov, S. I. Simak, B. Johansson, A. V. Ruban, and H. L. Skriver, Phys. Rev. B **56**, 9319 (1997).
[31] J. Staunton, B. L. Gyorffy, A. J. Pindor, G. M. Stocks, and H. Winter, J. Magn. Magn. Mater. **45**, 15 (1984).
[32] B. L. Gyorffy, A. J. Pindor, J. B. Staunton, G. M. Stocks, and H. Winter, J. Phys. F: Met. Phys. **15**, 1337 (1985).
[33] J. P. Perdew and Y. Wang, Phys. Rev. B **45**, 13244 (1992).
[34] H. J. Monkhorst and J. D. Pack, Phys. Rev. B **13**, 5188 (1976).
[35] T. Mehaddene, O. Adjaoud, R. Kozubski, K. Tanaka, H. Numakura, J. M. Sanchez, Ch. Isso, W. Pfeiler, and V. Pierron-Bohnes, Scr. Mater. **53**, 435 (2005).
[36] W. Pfeiler, Acta Metall. **36**, 2417 (1988).
[37] S. L. Quimby and P. M. Sutton, Phys. Rev. **91**, 1122 (1953).
[38] M. A. Krivoglaz, *X-Ray and Neutron Diffraction in Nonideal Crystals* (Springer, Berlin, 1996).
[39] S. Y. Yu, B. Schönfeld, and G. Kostorz, Phys. Rev. B **56**, 8535 (1997).
[40] *International Tables for Crystallography*, Vol. C, edited by E. Prince (International Union of Crystallography, Chester, 2006).
[41] P. C. Clapp, Phys. Rev. B **4**, 255 (1971).
[42] V. Gerold and J. Kern, Acta Metall. **35**, 393 (1987).
[43] A. Kussmann and K. Jessen, Zeitschrift für Metallkunde **54**, 504 (1963).
[44] P. A. Korzhavyi, A. V. Ruban, J. Odqvist, J. O. Nilsson, and B. Johansson, Phys. Rev. B **79**, 054202 (2009).
[45] O. I. Gorbatov, I. K. Razumov, Yu. N. Gornostyrev, V. I. Razumovskiy, P. A. Korzhavyi, and A. V. Ruban, Phys. Rev. B **88**, 174113 (2013).
[46] M. Rahaman, A. V. Ruban, A. Mookerjee, and B. Johansson, Phys. Rev. B **83**, 054202 (2011).
[47] J. M. Sanchez, Phys. Rev. B **81**, 224202 (2010).
[48] D. M. C. Nicholson, R. I. Barabash, G. E. Ice, C. J. Sparks, J. L. Robertson, and C. Wolverton, J. Phys.: Condens. Matter **18**, 11585 (2006).
[49] A. V. Ruban and I. A. Abrikosov, Rep. Prog. Phys. **71**, 046501 (2008).